

# Core-Shell Au@Ag Nanoparticles Synthesized with Polyphenols as Antimicrobial Agents

**Jesús Mauro Adolfo Villalobos-Noriega**

Universidad de Sonora

**Ericka Rodríguez Leon**

Universidad de Sonora

**César Rodríguez-Beas**

Universidad de Sonora

**Eduardo Larios-Rodríguez**

Universidad de Sonora

**Maribel Plascencia-Jatomea**

Universidad de Sonora Division de Ciencias Biologicas y de la Salud

**Aarón Martínez-Higuera**

Universidad de Sonora

**Heriberto Acuña-Campa**

Universidad de Sonora

**Ramón Alfonso Iñiguez-Palomares** (✉ [ramonalfonso.iniguez@gmail.com](mailto:ramonalfonso.iniguez@gmail.com))

Universidad de Sonora <https://orcid.org/0000-0002-9218-936X>

---

## Nano Express

**Keywords:** Green synthesis, Au@Ag core@shell nanoparticles, Rumex hymenosepalus, microorganisms, polyphenols, Gompertz model, Lag Phase

**Posted Date:** January 18th, 2021

**DOI:** <https://doi.org/10.21203/rs.3.rs-145053/v1>

**License:**  This work is licensed under a Creative Commons Attribution 4.0 International License.

[Read Full License](#)

---

**Version of Record:** A version of this preprint was published at Nanoscale Research Letters on July 22nd, 2021. See the published version at <https://doi.org/10.1186/s11671-021-03572-5>.

# Abstract

In this work, we used a sequential method of synthesis for gold-silver bimetallic nanoparticles with core@shell structure (Au@AgNPs). *Rumex hymenosepalus* root extract (Rh), which presents high content in catechins and stilbenes, was used as reductor agent in nanoparticles synthesis. Size distribution obtained by Transmission Electron Microscopy (TEM) give a diameter mean of 36 nm for Au@AgNPs, and 24 nm for gold nanoparticles (AuNPs). The geometrical shapes of NPs were principally quasi-spherical. The thickness of silver shell over AuNPs are around 6 nm and covered by active biomolecules onto surface. Microstructural characterization included high angle annular dark field images (HAADF) recorded with a scanning transmission electron microscope (STEM), Energy-Dispersive X-ray Spectroscopy (EDS), X-Ray Diffraction (XRD), UV-Vis Spectroscopy, and Zeta Potential. Also, a growth kinetic curve analysis using the Gompertz model for *Staphylococcus aureus* (Gram-positive), *Escherichia coli* (Gram-negative), and *Candida albicans* (yeast) were carried out for Au@AgNPs and monometallic AuNPs and AgNPs. Interestingly, Gompertz analysis indicates that Au@AgNPs present a higher effect on the growth kinetic of microorganisms than shown by monometallic nanoparticles.

## Introduction

In the last 25 years, several chemical methods have been studied for nanomaterial synthesis; however, most of these methods use substances that are unfriendly to the environment and use high temperatures or expensive equipment. In this work, we performed the synthesis of gold-silver nanostructures by using the green synthesis method. This method minimizes pollution from the beginning. Using "clean" processes, avoiding most of the waste and use of hazardous pollutants in developing "clean" nanomaterials that do not pose a threat to health or the environment.

Green synthesis of metal nanoparticles seeks a positive influence of the interaction with biological systems, which means that nanoparticles and their self-functionalization with polyphenol molecules generate biological interactions compatible with systems such as cells and macromolecules. In general, these biological interactions are used as nanomedicine for diseases such as cancer, diabetes, and neurodegenerative diseases. The synthesis of silver (shell) and AuNPs as a core-shell system [1] have applications such as optical diagnostic sensors, photothermal therapies, antimicrobials and improves the catalytic process [2] compared with monometallic NPs.

In particular, sequential or simultaneous methods in different reactors are used for the bimetallic synthesis: a microfluidic chip [3], sequential nanofluidic nanoprecipitation [4, 5] microemulsions[6], liposomes [7], reducing agents used are chemical or green chemical types.

Antibacterial properties of bimetallic nanomaterials [8–12] improve as a function of the concentration of Ag. In contrast, an increment in Au concentration decreases the antibacterial properties but reduces the cytotoxic effect, i.e., the bimetallic material becomes more biocompatible [13]. Comparing the effect of Au

and Ag monometallic materials with bimetallic materials [14–18], it has been demonstrated that a synergistic effect [19] occurs between bimetallic materials, generating bifunctional effects [20, 21].

Nanomaterials functionalization has particular interest since the chemical environment (pH, presence of sulfur, biocompatible molecules, etc.) surrounding the system will have effects on the interaction with cells or microorganisms; therefore, the emphasis on generating biomaterials using green chemistry [22–31].

The chemical composition of the bimetallic particles [32, 33] will be a determining factor in their optical properties [19], owing to the synergistic effect of monometallic nanostructures [34].

In this work, gold and silver nanoparticles were synthesized using as a reductor agent a *Rumex hymenosepalus* extract, which is a plant that contains stilbenes and catechins molecules that act as powerful antioxidants in reducing metal ions. Gold nanoparticles were used as nuclei to obtain bimetallic nanoparticles core@shell type of Au@Ag through a sequential synthesis method. The characterization of nanomaterials involves the techniques of HAADF-STEM, TEM with EDS y HRTEM.

With the different types of synthesized nanoparticles, a comparative study was carried out on the growth dynamics of the bacteria *E. coli* and *S. aureus* and the yeast *Candida albicans*.

## Experimental Section

### Materials

Rh extract was obtained under the conditions reported by Rodríguez et al. [35]. Both precursors  $\text{HAuCl}_4$  and  $\text{AgNO}_3$  for nanoparticle synthesis were purchased from Sigma-Aldrich with a purity of 99%. Brain Heart Infusion (BHI) Broth and Potato Dextrose Broth (PDB) used for microorganism assays were procured from Sigma-Aldrich. Ethanol (99% pure) used on the cleaning nanoparticles process was acquired from Fermont, and ultrapure water (milli-Q) was used on experiments.

### Synthesis of AuNPs

Firstly, *Rumex hymenosepalus* aqueous solution was prepared at 10 mg/mL from the lyophilized extract. Later 16mL of *Rumex* solution was mixed with 32mL of ultrapure water, keeping agitation at 1000 rpm, and were added slowly 16 mL of  $\text{HAuCl}_4$  (0.01 M). The reaction was held for 1 hour under laboratory lighting conditions and at room temperature. The intensity of surface plasmon resonance ( $\lambda_{\text{SPR}}=540$  nm) was evaluated by UV-vis spectroscopy over time; when no change was observed, the synthesis was considered complete. The obtained product was centrifuged at 12,000 rpm, the supernatant was replaced by ultrapure water, and a sonication process was applied for 1h to redisperse nanoparticles. The procedure was repeated three times more. Water was used as a solvent on the first two occasions and ethanol on the last. Finally, ethanolic dispersion was centrifuged, and precipitates dried in a convection oven at 40 to prepare an AuNPs aqueous dispersion at 2300  $\mu\text{g/mL}$ .

## Synthesis of Au@AgNPs

For Au@AgNPs synthesis, 2 ml of the AuNPs aqueous dispersion (2300 µg/mL), 0.8 mL of AgNO<sub>3</sub> (0.1 M), and 0.8 mL of *Rumex hymenosepalus* solution (10 mg/mL) were deposited in a sterile glass culture tube. The mixture was sonicated for 3 h in an ultrasonic cleaner bath (Branson, Model 2510). Later, the content was centrifuged at 12,000 rpm for one hour, solids obtained were redispersed in ultrapure water by sonication.

## Synthesis of AgNPs

AgNPs were synthesized following the protocol described by Rodríguez et al. [35], and a similar size of AgNPs was obtained. Monometallic nanoparticles (AgNPs and AuNPs) were synthesized to compare the effects concerning Au@Ag bimetallic nanoparticles over the growth kinetics of microorganisms.

## UV-Vis Spectroscopy

UV-Vis absorption spectra were obtained on a dual-beam Perkin Elmer Lambda 45 spectrometer. A slit of 0.5 nm was employed, and spectra were recorded at a speed of 480 nm/min in a range between 200 and 900 nm. For the nanoparticles, 50 µL of sample and only 5 µL for the extract were used. The final volume was made up to 3mL in the quartz cells using ultra-pure water as solvent.

## Z-Potential

Zeta potential ( $\zeta$ ) of AuNPs, AgNPs, and Au@AgNPs were measured using a Zetasizer-Nano ZS (Malvern Instruments, UK). Each sample was measured at room temperature (25°C) in triplicate.

## HAADF-STEM

High-Angle Annular Dark Field-Scanning Transmission Electron Microscopy (HAADF-STEM) can be considered a powerful operation mode in electron microscopy, which provides a large amount of complementary information elucidates the structure of a nanomaterial. Aberration-corrected HAADF-STEM can determine with atomic resolution the positions of atoms of different chemical nature. This is due to aberration-corrected HAADF-STEM, known for its chemical sensitivity and high spatial resolution [35]. In this operation mode, the incoherent image is dominant with a negligible contribution of diffraction contrast [36–38]. Thus, atomic number contrast (Z contrast) in HAADF-STEM aberration-corrected allows us to determine the structural details of nanostructures with great precision.

For STEM analysis, samples were analyzed in a JEOL-JEMARM200 electron microscope operating at 200 kV, with a CEOS-corrector for the condenser lens. Z-Contrast STEM images were recorded simultaneously in both BF and HAADF modes. Images were recorded with a 40-micron condenser lens aperture (32-36 mrad convergence angle) and a spot size of 9 pA.

For electron microscopy analysis, a drop (10  $\mu\text{L}$ ) of Au@AgNPs suspension was deposited on a 300-mesh thick carbon grid, dried to room temperature, and placed in a vacuum chamber for 24 h.

### **TEM, HRTEM, and EDS**

Nanoparticles were analyzed by TEM in Jeol 2010F apparatus (1.9 Å resolution) at 200kV. EDS analysis was realized using a QUANTAX 200-TEM X-ray spectrometer (Bruker) with XFlash 4010 detector. For HRTEM analysis, TEM micrographs were recorded at magnifications greater than 100,000X. Interplanar spacings of crystal planes were determined by digital micrograph analysis (3.0 Gatan Version). Sample preparation was similar to that described above for STEM analysis.

### **XRD**

Data were collected using a Bruker D8 QUEST diffractometer system equipped with a Multilayer mirrors monochromator and a Cu K $\alpha$  Microfocus sealed tube ( $\lambda=1.54178$  Å). Frames were collected at T=300 K via  $\omega/\varphi$ -scans and then processed to obtain diffractograms of Intensity vs. 2Theta. High Score Plus software was used for raw data treatment and the ICSD powder diffraction database associated with software was implemented for the search-match phase identification analyses.

### **Antibacterial Activity Assay**

Microorganisms tested were: bacteria *Escherichia coli* (ATCC 25922), *Staphylococcus aureus* (ATCC 5538P), and yeast *Candida albicans* isolated from infected urine collected from an adult male patient with urinary tract infection (our study follow the principles of the Declaration of Helsinki). Brain Heart Infusion (BHI) and Potato Dextrose Broth (PDB) were used to prepare inoculum of bacteria and yeast, respectively. Cultures were incubated at 37 °C overnight. The concentration in colony-forming units (CFU/mL) per milliliter of suspension was determined by measuring the optical density by UV-Vis at 540 nm for bacteria, 600 nm for yeast. Suspensions containing  $4 \times 10^8$ ,  $7.8 \times 10^8$ , and  $2.5 \times 10^6$  CFU/mL were used for *E. coli*, *S. aureus*, and *C. albicans*, respectively. Antimicrobial activity was tested in 96-well plates, using liquid culture medium added with nanoparticles and microorganism at 37 °C. All tests were performed by triplicate. Absorbance was measured in a multimode plate reader Synergy HTX Biotek, using Gen 5 software. All the microbial growth curves were performed using the Origin Lab 8.0 software. As a first step, 70  $\mu\text{L}$  of fresh broth medium (BHI or PDB, according to the studied microorganisms) mixed with nanoparticles at the required concentration were added to the wells. Later, 30  $\mu\text{L}$  of microorganism suspension was added to the wells and homogenized with the medium. The final volume on each well was 100  $\mu\text{L}$ . After dispensing the inoculum, the 96-well plates were read in the spectrophotometer described above. Plates were kept at 37 °C for 24 h, with a circular shaking mode before each reading with a period of 15 min each. The growth rate of microorganisms was determined by optical density measurement (OD) at the mentioned wavelength.

### **Curves Growth analyzed by the Gompertz model**

It is well known in the literature that the Gompertz growth model well describes the growth of microorganism populations. This model allows us to understand two critical parameters in the description of the growth of the microorganism population: the adaptive phase (Lag phase) and the population growth rate. In particular, studying the behavior of the Lag phase in inhibitory treatments of microorganisms is relevant because it provides information on the adaptive responses of the microorganism to the treatment and can even give indications about the development of resistance of the microorganism to the evaluated treatment [39].

Modified Gompertz model has been described by Zwietering et al. [40] and adapted by Li et al. [39] and other authors [41–48] as a model that adjust the growth curves and

$$y = A \exp \left\{ -\exp \left[ \frac{\mu e}{A} (\lambda - t) + 1 \right] \right\} \quad \text{Equation 1}$$

Where,  $A$  is the cell number expressed as  $OD_{540}$  (*S. aureus* and *E. coli*) and  $OD_{600}$  (*C. albicans*),  $\mu$  is the growth rate at the exponential phase and  $e$  is the exponential  $e^1$ ,  $\lambda$  is the lag phase. We have adjusted our growth kinetic using a software origin 9.1 to analyze the effects over *S. aureus*, *E. coli*, and *C. albicans* of the three agents AuNPs, AgNPs, and Au@AgNPs.

## Results And Discussion

### UV-Vis Spectroscopy and Z-potential

Figure 1 (A) shows the UV-vis absorption spectra of the synthesized nanomaterials. The absorbances have been normalized for the maximum localized surface plasmon resonance (LSPR) corresponding to each nanoparticle system.

Au@AgNPs absorption spectrum in Figure 1 has a single band centered at 474 nm, which almost covers the entire region of the experiment. The wavelength of the LSPR for Au@AgNPs is located between the AgNPs LSPR (445 nm) and the AuNPs LSPR (544 nm). The absence of a gold-like absorption peak on Au@AgNPs suggests that obtained nanomaterials by sequential synthesis are core@shell structures. It is not possible to detect any absorption band associated with Au belongs to the nucleus. Some authors assume that for core@shell systems, the absorption spectra are composed of two bands associated with each of the metals for shell thicknesses between 3 and 4 nm. The absorption associated with metalcore disappears for higher thicknesses, obtaining a single absorption band where the maximum location depends on the thickness/core size ratio of the bimetallic particle [49, 50].

Samal et al. [51] synthesized core @ shell nanoparticles (Au@Ag) by controlling the nuclei sizes and adding different thicknesses shells. In particular, our UV-vis result for Au@AgNPs coincides with that reported by Samal et al. for 32 nm gold cores and a silver thickness greater than 15 nm, where spectra are characterized by a single absorption band (~ 450 nm), and the suppression of Au surface plasmons are observed.

Additionally, in Figure 1A, absorption centered at 280 nm (region highlighted in blue) can be observed, corresponding to molecules from the *Rumex hymenosepalus* extract used as a reducing agent in our nanoparticle synthesis. Figure S1 corresponds to *Rumex hymenosepalus* aqueous solution absorption spectrum. A characteristic band centered at 278nm is observed, associated with the electronic transitions of the aromatic rings conjugated with the carbonyl groups of polyphenolic compounds [52]. This absorption band in the nanoparticles UV-Vis spectra indicates that final products contain extract molecules that remain in them.

Figures 1B, 1C, and 1D show the average curves of Z potentials corresponding to AuNPs, AgNPs, and Au@AgNPs. The graphs show a Gaussian behavior with peaks centered at -49.7mV, -47.2mV, and -51.3mV, respectively. These highly negative Z potential values indicate that nanoparticles experience repulsive interactions between them that prevent their aggregation and allow the long-term stability of metal colloids [53–55]. By correlating the UV-vis spectroscopy results with the obtained Z potential values, we can establish that the highly negative values may be due to the complexing of polyphenolic molecules of the extract onto the nanoparticle surface [56].

## HAADF-STEM

Figure 2A corresponds to a representative bright-field STEM micrograph of the Au@AgNPs system at low magnification (100 nm scale bar). A set of nanoparticles without agglomeration and with mostly quasi-spherical geometry can be seen. The same region is shown in dark field (HAADF) in Figure 2B, and the core@shell structure can be observed, where can we distinguish Au-core looks more intense than Ag-shell, due to the difference in atomic number. Figures 2C and 2D correspond to STEM higher magnification micrograph (scale bare 20nm) of a nanoparticles group of system core@shell in a bright and dark field, respectively. Can be appreciated with clarity brilliant Au core and Ag shell lightly contrasted. These images show that the thickness of Ag-shell varies between 3 and 5 nm. Figure S2 corresponds to an individual images gallery where can be observed uniformity of Ag-shell.

## TEM, HRTEM, and EDS

Figures 3A, 3C, and 3E correspond to micrograph TEM of representative nanoparticles systems AuNPs, AgNPs, and Au@AgNPs, respectively. In all cases, nanoparticles have sphere-like morphology and are shown well separated from each other. This can be explained by the extract molecules onto nanoparticle surfaces, acting as spacers between them. Figure 3B, 3D, and 3F are shown histograms correspond to size distribution obtained by TEM and performed with 500 nanoparticles. The histogram presents Gaussian distribution with a mean size of  $24.23 \pm 3.78\text{nm}$  (AuNPs),  $13.20 \pm 2.81\text{nm}$  (AgNPs), and  $36.19 \pm 11.09\text{nm}$  (Au@AgNPs).

For biological applications, it is valuable to obtain nanoparticles population with monodisperse sizes[57], so that dispersity was calculated from TEM data as reported by Tiunov et al. [58]. Polydispersity values obtained are 0.156, 0.212, and 0.306 for AuNPs, AgNPs, and Au@AgNPs, respectively, which correspond to the nanoparticles population of highly homogeneous sizes [59].

Figure 4 corresponds to the Au@AgNPs HAADF-STEM micrographics. A single nanoparticle is shown in figure 4A with a gold nucleus and silver cover perfectly delimited. The red square region is amplified to obtain an HRTEM micrograph of the shell portion (Figure 4B), then to verify the crystalline shell structure, the nanoparticle periphery region was analyzed (discontinued square) with the Digital Micrograph 3.0 software (Gatan). Fast Fourier Transform (FFT) image of the selected area was obtained (Figure 4C). Using the Inverse Fast Fourier Transform was possible to estimate interplanar distances of 2.3 Å, 2.0 Å, and 1.4 Å in Figure 4D. These distances can be assigned respectively to the crystalline planes (111), (200), and (220) of face-centered cubic (fcc) silver according to Powder Diffraction File Card 00-004-0783 [60]. A similar analysis of crystal structure by HRTEM was carried out for monometallic nanoparticles as illustrated in Figures S4 (for AuNPs) and S5 (AgNPs). In both cases, crystal structure corresponds to face-centered cubic (fcc).

## EDS

EDS chemical analysis shows the presence of both metals for a group of bimetallic Au@AgNPs observed by TEM (Figure 5A) in proportions of the atomic weight percent 77% of Ag (shell) and 23% of Au (cores) (Figure 5B). In comparison, a single bimetallic (Figure 5C) Au@AgNPs has proportions around 80% of Ag (shell) and 20% of Au (core) (Figure 5D).

These results are coincident with estimations effectuated (considering quasi-spherical NPs) for the Au and Ag content from the experimental results of size measurement by TEM for AuNPs and its corresponding Au@AgNPs; our calculations give an atomic content of 70.68 % for Ag (shell) and 29.32% (core).

## XRD

Figure 6 corresponds to XRD patterns for AuNPs and AgNPs as well as bimetallic Au@AgNPs. All the synthesized products have fcc crystalline structure as previously reported in the characterization by electron microscopy. Peaks for Au@AgNPs are located at  $2\theta$  diffraction angles of 38.25 °, 44.4 °, 64.9 °, 77.85 °, and 81.25 °. As can be appreciated in the figure, the AgNPs and AuNPs diffraction peaks are found in the same positions mentioned with a difference of  $\pm 0.5$  °. This is because Au and Ag have very similar lattice constants, so their diffraction patterns for fcc crystal structure are almost identical (REF: Green synthesis and applications of Au–Ag bimetallic nanoparticles). In this way, the diffraction peaks in figure 6 are assigned, respectively, to the crystalline planes (111), (200), (220), (311) and (222) of the gold and silver fcc structure in accordance with ICSD #180868 and ICSD #604631.

## Antimicrobial Activity

Monometallic (AgNPs, AuNPs) and bimetallic (Au@AgNPs) materials were tested at four different concentrations: 1, 10, 50, and 100 µg/mL. Selected microorganisms to evaluate antimicrobial activity were yeast *Candida albicans*, Gram positive bacteria *S.aureus*, and Gram negative bacteria *E. coli*. Growth kinetics curves in a time-lapse of 24 h are shown in Figure 7.

### ***C. albicans***

AuNPs show no effect on growth kinetics until 10 h (Figure 7A), varying in a dose-dependent manner the absorbance reached at 24 h. Interestingly, with 50  $\mu\text{g}/\text{mL}$  or more, the growth kinetic shows a steep negative slope from 10 h until reaching a 45% reduction at 24 h, which suggests an antifungal effect of these materials. This can be attributed to the ability of gold nanoparticles to interact with relevant proteins present in fungus such as  $\text{H}^+$ -ATPase, affecting proton pump activity. This atrophying the ability of yeast to incorporate nutrients causing its death [61]. In Figures 7B and 7C was observed that AgNPs and Au@AgNPs inhibit the growth of the yeast *Candida albicans* from 10  $\mu\text{g}/\text{mL}$ . The determination of the  $\text{MIC}_{50}$  concentration for both materials was estimated from the dose-response curve shown in Figure S5.  $\text{MIC}_{50}$  is defined as the concentration of nanoparticles that produces a 50% decrease in absorbance concerning the control (yeast without treatment). For AgNPs and Au@AgNPs,  $\text{MIC}_{50}$  were 2.21  $\mu\text{g}/\text{mL}$  and 2.37  $\mu\text{g}/\text{mL}$ , respectively.

However, according to the EDS results (Figure 7B), the silver content in Au@AgNPs is 64.85% mass. Thus, the concentration of silver in Au@AgNPs for  $\text{MIC}_{50}$  is 1.53  $\mu\text{g}/\text{mL}$ , 30% lower than in the case of AgNPs.

### ***E coli***

In Figure 7D, AuNPs do not show significant inhibition (<15%) or affect the growth kinetics of *E.coli*. For AgNPs (Figure 7E) at low concentrations, the Lag phase remains unchanged, but there is a marked decrease in growth ratio indicated by the slope decrement. At 50  $\mu\text{g}/\text{mL}$  Lag phase lasts up to 16 h and viability reaches a maximum of 20% at 24 h. For 100  $\mu\text{g}/\text{mL}$ , an apparent detachment of the growth phase of the microorganism is not observed. In Au@AgNPs (Figure 7F), the first two concentrations do not show changes in their growth phase, but a phase delay of up to 2 h is observed compared to the control. It is interesting to note that the lag phase lasts up to 21 h for the 50  $\mu\text{g}/\text{mL}$  concentration, finally there is no explicit growth behavior for the 100  $\mu\text{g}/\text{mL}$  concentration.

### ***S. aureus***

A comparative analysis of lag phase regrowth occurred after 12 h for Au (Figure 7G), Ag (Figure 7H), and Au@AgNPs (Figure 7I) in the case of *S. aureus* at 50  $\mu\text{g}/\text{mL}$ . For the highest concentration at 100  $\mu\text{g}/\text{mL}$ , there is no growth of the bacteria. Additionally, we observe changes in the slope of respect control for Au, Ag, and Au@AgNPs at 1 and 10  $\mu\text{g}/\text{mL}$ .

AuNPs interaction with these Gram-positive bacteria could be due to the charged surface that causes an electrostatic interaction, destabilizing membrane structure. Similar results, but with higher NPs concentrations are reported for AuNPs synthesized using Ananas comosus fruit extract as reducing agent [62] and blue-green alga *Spirulina platensis* protein [63]. Yang et al. show  $\text{MIC} > 500 \mu\text{g}/\text{mL}$  for *S. aureus* (CMCC(B)26003), our AuNPs has shown inhibition with 10 times less concentration, in this case, a critical synergy exists with polyphenols molecules on coating and stabilizing the surface of nanoparticle [64]. ROS is generated of less to higher intensity [65] by AuNPs, polyphenols (plant extracts), and AgNPs, so

AuNPs in synergy with resveratrol and EGCG promotes antibacterial response over *S. aureus* [66] had the most feasible mechanism in this case. Penders et al. reported 250 and 500  $\mu\text{g}/\text{mL}$  of AuNPs like antibacterial agents over *S. aureus* increases in bacterial growth lag time and antibacterial effect [62, 63, 67].

We believe that inhibition is caused by AgNPs accumulation and diffusion on bacteria related to NPs surface charges that promote electrostatic interactions [68] with the bacteria's membrane leading to higher penetration and damage. We think this is a similar mechanism described for interactions between *E. coli* biofilms and AgNps [69].

For Au@AgNPs, the obtained results are comparable to those reported by other workgroups [64, 65]; however, different authors suggest that the inhibition of the growth of the microorganisms is directly related to the thickness of the shell [64, 65]. Core-shell NPs showed low cytotoxicity when tested in NIH-3T3 fibroblasts cells (normal mammalian cells) [62]. A lower proportion of silver in the shell of the Au@AgNPs shows similar results to AgNPs [64], Au core potentialize antibacterial effect, and minimize the cytotoxicity.

### **Curves Growth analyzed by the modified Gompertz model**

To know how the growth ratios ( $\mu$ ) and Lag phase ( $\lambda$ ) are quantitatively modified, the growth curves of microorganisms exposed to different concentrations of nanomaterials (Figure 7) were adjusted by the Gompertz model (Eq. 1).

In Figure 8A, it can be seen that all nanomaterials produce a decrease in the replication rate of *S. aureus* populations when the concentration of nanoparticles increases. This effect results in slightly higher sensitivity for AuNPs. At a concentration of 50  $\mu\text{g}/\text{mL}$ , the growth ratio is only 30% concerning control (Table S1-S24); at a concentration of 100  $\mu\text{g}/\text{mL}$ , all materials inhibit the growth of the *S. aureus* population. The behavior of the adaptive phase for *S. aureus* with the different treatments is shown in Figure 8B. It is observed that there are no significant differences in the material used, and at 50  $\mu\text{g}/\text{mL}$ , the Lag phase has increased by almost 5 times compared to the adaptive phase of *S. aureus* (Tables S1-S24). In general, we can establish that the different nanomaterials evaluated in *S. aureus* reduce the replication rate and postpone the adaptive phase in a dose-dependent manner until its inhibition at 100  $\mu\text{g}/\text{mL}$ .

Figure 8C clearly shows that AuNPs do not affect the growth ratio  $\mu$  of *E. coli* bacteria. Meanwhile, AgNPs produce a decrease over  $\mu$ , reaching a minimum value corresponding to 19% to the control ( $\mu$  for *E. coli* without treatment) for 50  $\mu\text{g}/\text{mL}$  (see table S52). In contrast, Au@AgNPs completely inhibit the *E. coli* growth at 100  $\mu\text{g}/\text{mL}$ . Analysis of the behavior of *E. coli* Lag phase exposed to different materials is shown in Figure 8D. In this case, unlike Figure 8B, each material has a characteristic response. Thus, AuNPs do not generate any modification in the adaptive phase of *E. coli*, while AgNPs and Au@AgNPs have a dose-dependent effect on the Lag phase, the latter material standing out. Thus, we can establish that AuNPs have no appreciable effect on *E. coli* bacteria, and Au@AgNPs can inhibit replication and,

therefore, indefinitely postpone the Lag phase of *E.coli*. Interestingly, this effect is not achieved for AgNPs even though the net silver content is higher than in Au@AgNPs. This suggests that the core@shell presentation of both metals produces a synergy that favors antimicrobial activity.

## Conclusions

For the first time, the production of gold nanoparticles and core@shell (Au@Ag) is reported using a *Rumex hymenosepalus* root extract as a reducing agent. To obtain Au@AgNPs is proposed a two-step sequential method that produces particles with low polydispersity and homogeneous silver shell. Determination of the growth curves and their parameters obtained through the Gompertz model indicate different effects of the nanomaterials on evaluated microorganisms. Inhibitory effects of AuNPs over *S. aureus* are reached at a concentration of 5 times less to reported for other AuNPs synthesized by different processes. This reveals the importance of the synthesis process followed and the environment on the surface of the nanoparticles. On the other hand, AgNPs and Au@AgNPs produce a great growth of the lag phase (> 12 hrs). However, bacteria can adapt and initiate their growth at these sub-inhibitory concentrations with the consequent risk of generate resistance to these nanomaterials. This highlights the importance of conducting growth kinetic studies that cover an appropriate period of time to discard a delayed growth. Interestingly, Gompertz analysis indicates that Au@AgNPs present a higher effect on the growth kinetic of microorganisms than shown by monometallic nanoparticles, which can be attributed to a synergistic effect of both metals on the core@shell structure.

## Declarations

### Conflicts of interest

The authors declare no competing financial interest.

### Acknowledgments

All authors wish to thank Dr. José Yacamán for the facilities provided in the characterization of the systems by electronic microscopy, as well as to the Kleberg Advanced Microscopy Center of the University of Texas at San Antonio Physics and Astronomy and to the Laboratory of Biomaterials of Physics Department, University of Sonora. The authors are also grateful for the support of the SAGARPA projects 17-PFA-IIDTTT-001448-L000-DF, as well as the support provided by the Secretariat of Public Education (SEP) through PRODEP (Programa para el Desarrollo Profesional Docente) by the Postdoc fellowship 0511-6/17-4022 and AMH would like to thank Conacyt for Post-Doctoral Fellowship (2019-000019-01NACV-00449), Support number 740180.

## References

1. Chen Y-H, Yeh C-S (2001) A new approach for the formation of alloy nanoparticles: laser synthesis of gold–silver alloy from gold–silver colloidal mixtures. *Chem Commun (Camb)* 371–372

2. Gaines TW, Williams KR, Wagener KB (2016) ADMET. In: Petrochemical Catalyst Materials, Processes, and Emerging Technologies. IGI Global, pp 1–21
3. Zhang L, Feng Q, Wang J, et al (2015) Inside cover: Microfluidic synthesis of rigid nanovesicles for hydrophilic reagents delivery (angew. Chem. Int. Ed. 13/2015). *Angew Chem Int Ed Engl* 54:3830–3830
4. Liu D, Zhang H, Cito S, et al (2017) Core/shell nanocomposites produced by superfast sequential microfluidic nanoprecipitation. *Nano Lett* 17:606–614
5. Sebastián V, Zaborenko N, Gu L, Jensen KF (2017) Microfluidic assisted synthesis of hybrid Au–pd dumbbell-like nanostructures: Sequential addition of reagents and ultrasonic radiation. *Cryst Growth Des* 17:2700–2710
6. Zaleska-Medynska A, Marchelek M, Diak M, Grabowska E (2016) Noble metal-based bimetallic nanoparticles: the effect of the structure on the optical, catalytic and photocatalytic properties. *Adv Colloid Interface Sci* 229:80–107
7. Lee J-H, Shin Y, Lee W, et al (2016) General and programmable synthesis of hybrid liposome/metal nanoparticles. *Sci Adv* 2:e1601838
8. Franci G, Falanga A, Galdiero S, et al (2015) Silver nanoparticles as potential antibacterial agents. *Molecules* 20:8856–8874
9. Thanh NTK, Green LAW (2010) Functionalisation of nanoparticles for biomedical applications. *Nano Today* 5:213–230
10. Karam TE, Smith HT, Haber LH (2015) Enhanced photothermal effects and excited-state dynamics of plasmonic size-controlled gold–silver–gold core–shell–shell nanoparticles. *J Phys Chem C Nanomater Interfaces* 119:18573–18580
11. Ding X, Yuan P, Gao N, et al (2017) Au-Ag core-shell nanoparticles for simultaneous bacterial imaging and synergistic antibacterial activity. *Nanomedicine* 13:297–305
12. Paszkiewicz M, Gołębiewska A, Rajski Ł, et al (2016) Synthesis and characterization of monometallic (Ag, Cu) and bimetallic Ag-Cu particles for antibacterial and antifungal applications. *J Nanomater* 2016:1–11
13. Padmos JD, Langman M, MacDonald K, et al (2015) Correlating the atomic structure of bimetallic silver–gold nanoparticles to their antibacterial and cytotoxic activities. *J Phys Chem C Nanomater Interfaces* 119:7472–7482
14. Peng X, Pan Q, Rempel GL (2008) Bimetallic dendrimer-encapsulated nanoparticles as catalysts: a review of the research advances. *Chem Soc Rev* 37:1619–1628
15. Toshima N, Yonezawa T (1998) Bimetallic nanoparticles—novel materials for chemical and physical applications. *New J Chem* 22:1179–1201
16. Scott RWJ, Wilson OM, Oh S-K (2004) Bimetallic Palladium–Gold Dendrimer-Encapsulated Catalysts
17. Mondal S, Roy N, Laskar RA, et al (2011) Biogenic synthesis of Ag, Au and bimetallic Au/Ag alloy nanoparticles using aqueous extract of mahogany (*Swietenia mahogani* JACQ.) leaves. *Colloids*

18. TamIn situ biosynthesis of Ag, Au and bimetallic nanoparticles using *Piper pedicellatum* C. Green chemistry approach, DC
19. Roopan SM, Surendra TV, Elango G, Kumar SHS (2014) Biosynthetic trends and future aspects of bimetallic nanoparticles and its medicinal applications. *Appl Microbiol Biotechnol* 98:5289–5300
20. Banerjee M, Sharma S, Chattopadhyay A, Ghosh SS (2011) Enhanced antibacterial activity of bimetallic gold-silver core-shell nanoparticles at low silver concentration. *Nanoscale* 3:5120–5125
21. Huo D, He J, Li H, et al (2014) Fabrication of Au@Ag core-shell NPs as enhanced CT contrast agents with broad antibacterial properties. *Colloids Surf B Biointerfaces* 117:29–35
22. Roy N, Mondal S, Laskar RA, et al (2010) Biogenic synthesis of Au and Ag nanoparticles by Indian propolis and its constituents. *Colloids Surf B Biointerfaces* 76:317–325
23. Begum NA, Mondal S, Basu S, et al (2009) Biogenic synthesis of Au and Ag nanoparticles using aqueous solutions of Black Tea leaf extracts. *Colloids Surf B Biointerfaces* 71:113–118
24. Song JY, Kim BS (2008) Biological synthesis of bimetallic Au/Ag nanoparticles using Persimmon (*Diopyros kaki*) leaf extract. *Korean J Chem Eng* 25:808–811
25. Kasthuri J, Veerapandian S, Rajendiran N (2009) Biological synthesis of silver and gold nanoparticles using apiin as reducing agent. *Colloids Surf B Biointerfaces* 68:55–60
26. Joerger R, Klaus T, Granqvist CG (2000) Biologically produced silver–carbon composite materials for optically functional thin-film coatings. *Adv Mater* 12:407–409
27. Schabes-Retchkiman PS, Canizal G, Herrera-Becerra R, et al (2006) Biosynthesis and characterization of Ti/Ni bimetallic nanoparticles. *Opt Mater (Amst)* 29:95–99
28. Philip D (2009) Biosynthesis of Au, Ag and Au-Ag nanoparticles using edible mushroom extract. *Spectrochim Acta A Mol Biomol Spectrosc* 73:374–381
29. Huang J, Li Q, Sun D, et al (2007) Biosynthesis of silver and gold nanoparticles by novel sundried *Cinnamomum camphora* leaf. *Nanotechnology* 18:105104
30. Dwivedi AD, Gopal K (2010) Biosynthesis of silver and gold nanoparticles using *Chenopodium album* leaf extract. *Colloids Surf A Physicochem Eng Asp* 369:27–33
31. Castro-Longoria E, Vilchis-Nestor AR, Avalos-Borja M (2011) Biosynthesis of silver, gold and bimetallic nanoparticles using the filamentous fungus *Neurospora crassa*. *Colloids Surf B Biointerfaces* 83:42–48
32. Shin Y, Bae I-T, Arey BW, Exarhos GJ (2008) Facile stabilization of gold-silver alloy nanoparticles on cellulose nanocrystal. *J Phys Chem C Nanomater Interfaces* 112:4844–4848
33. An Q, Yu M, Zhang Y, et al (2012) Fe<sub>3</sub>O<sub>4</sub>@carbon microsphere supported Ag–Au bimetallic nanocrystals with the enhanced catalytic activity and selectivity for the reduction of nitroaromatic compounds. *J Phys Chem C Nanomater Interfaces* 116:22432–22440
34. Cheng Z-Q, Li Z-W, Yao R, et al (2020) Improved SERS performance and catalytic activity of dendritic Au/Ag bimetallic nanostructures based on Ag dendrites. *Nanoscale Res Lett* 15:117

35. Epicier T, Sato K, Tournus F, Konno T (2012) Chemical composition dispersion in bi-metallic nanoparticles: semi-automated analysis using HAADF-STEM. *J Nanopart Res* 14:. <https://doi.org/10.1007/s11051-012-1106-z>
36. Voyles PM, Muller DA, Grazul JL, et al (2002) Atomic-scale imaging of individual dopant atoms and clusters in highly n-type bulk Si. *Nature* 416:826–829
37. LeBeau JM, Findlay SD, Allen LJ, Stemmer S (2008) Quantitative atomic resolution scanning transmission electron microscopy. *Phys Rev Lett* 100:206101
38. Lebeau JM, Findlay SD, Allen LJ, Stemmer S (2010) Position averaged convergent beam electron diffraction: theory and applications. *Ultramicroscopy* 110:118–125
39. Li B, Qiu Y, Shi H, Yin H (2016) The importance of lag time extension in determining bacterial resistance to antibiotics. *Analyst* 141:3059–3067
40. Zwietering MH, Jongenburger I, Rombouts FM, van 't Riet K (1990) Modeling of the bacterial growth curve. *Appl Environ Microbiol* 56:1875–1881
41. Chatterjee T, Chatterjee BK, Majumdar D, Chakrabarti P (2015) Antibacterial effect of silver nanoparticles and the modeling of bacterial growth kinetics using a modified Gompertz model. *Biochim Biophys Acta* 1850:299–306
42. Penders J, Stolzoff M, Hickey DJ, et al (2017) Shape-dependent antibacterial effects of non-cytotoxic gold nanoparticles. *Int J Nanomedicine* 12:2457–2468
43. Lambert RJ, Pearson J (2000) Susceptibility testing: accurate and reproducible minimum inhibitory concentration (MIC) and non-inhibitory concentration (NIC) values. *J Appl Microbiol* 88:784–790
44. Dartevelle P, Ehlinger C, Zaet A, et al (2018) D-Cateslytin: a new antifungal agent for the treatment of oral *Candida albicans* associated infections. *Sci Rep* 8:. <https://doi.org/10.1038/s41598-018-27417-x>
45. Lomelí-Marroquín D, Medina Cruz D, Nieto-Argüello A, et al (2019) Starch-mediated synthesis of mono- and bimetallic silver/gold nanoparticles as antimicrobial and anticancer agents. *Int J Nanomedicine* 14:2171–2190
46. Chankaew C, Somsri S, Tapala W, et al (2018) Kaffir lime leaf extract mediated synthesis, anticancer activities and antibacterial kinetics of Ag and Ag/AgCl nanoparticles. *Particuology* 40:160–168
47. Hernández-Díaz JA, Garza-García JJO, Zamudio-Ojeda A, et al (2020) Plant-mediated synthesis of nanoparticles and their antimicrobial activity against phytopathogens. *J Sci Food Agric*. <https://doi.org/10.1002/jsfa.10767>
48. Tjørve KMC, Tjørve E (2017) The use of Gompertz models in growth analyses, and new Gompertz-model approach: An addition to the Unified-Richards family. *PLoS One* 12:e0178691
49. Sinha T, Ahmaruzzaman M (2015) A novel and greener approach for shape controlled synthesis of gold and gold–silver core shell nanostructure and their application in optical coatings. *Spectrochim Acta A Mol Biomol Spectrosc* 145:280–288

50. Chen HM, Liu RS, Jang L-Y, et al (2006) Characterization of core-shell type and alloy Ag/Au bimetallic clusters by using extended X-ray absorption fine structure spectroscopy. *Chem Phys Lett* 421:118–123
51. Samal AK, Polavarapu L, Rodal-Cedeira S, et al (2013) Size tunable Au@Ag core-shell nanoparticles: synthesis and surface-enhanced Raman scattering properties. *Langmuir* 29:15076–15082
52. Lopes LCS, Brito LM, Bezerra TT, et al (2018) Silver and gold nanoparticles from tannic acid: synthesis, characterization and evaluation of antileishmanial and cytotoxic activities. *An Acad Bras Cienc* 90:2679–2689
53. Saratale RG, Shin HS, Kumar G, et al (2018) Exploiting antidiabetic activity of silver nanoparticles synthesized using *Punica granatum* leaves and anticancer potential against human liver cancer cells (HepG2). *Artif Cells Nanomed Biotechnol* 46:211–222
54. Rezazadeh NH, Buazar F, Matroodi S (2020) Synergistic effects of combinatorial chitosan and polyphenol biomolecules on enhanced antibacterial activity of biofunctionalized silver nanoparticles. *Sci Rep* 10:19615
55. Ajitha B, Ashok Kumar Reddy Y, Sreedhara Reddy P (2015) Green synthesis and characterization of silver nanoparticles using *Lantana camara* leaf extract. *Mater Sci Eng C Mater Biol Appl* 49:373–381
56. Maddinedi SB, Mandal BK, Maddili SK (2017) Biofabrication of size controllable silver nanoparticles - A green approach. *J Photochem Photobiol B* 167:236–241
57. Johnston ST, Faria M, Crampin EJ (2018) An analytical approach for quantifying the influence of nanoparticle polydispersity on cellular delivered dose. *J R Soc Interface* 15:.  
<https://doi.org/10.1098/rsif.2018.0364>
58. Tiunov IA, Gorbachevskyy MV, Kopitsyn DS, et al (2016) Synthesis of large uniform gold and core-shell gold-silver nanoparticles: Effect of temperature control. *Russ J Phys Chem* 90:152–157
59. Neto DMA, Freire RM, Gallo J, et al (2017) Rapid sonochemical approach produces functionalized Fe<sub>3</sub>O<sub>4</sub> nanoparticles with excellent magnetic, colloidal, and relaxivity properties for MRI application. *J Phys Chem C Nanomater Interfaces* 121:24206–24222
60. Abdullah NISB, Ahmad MB, Shameli K (2015) Biosynthesis of silver nanoparticles using *Artocarpus elasticus* stem bark extract. *Chem Cent J* 9:61
61. Wani IA, Ahmad T, Manzoor N (2013) Size and shape dependant antifungal activity of gold nanoparticles: a case study of *Candida*. *Colloids Surf B Biointerfaces* 101:162–170
62. Bindhu MR, Umadevi M (2014) Antibacterial activities of green synthesized gold nanoparticles. *Mater Lett* 120:122–125
63. Suganya KSU, Govindaraju K, Kumar VG, et al (2015) Blue green alga mediated synthesis of gold nanoparticles and its antibacterial efficacy against Gram positive organisms. *Mater Sci Eng C Mater Biol Appl* 47:351–356
64. Yang L, Yan W, Wang H, et al (2017) Shell thickness-dependent antibacterial activity and biocompatibility of gold@silver core-shell nanoparticles. *RSC Adv* 7:11355–11361

65. Tsai T-T, Huang T-H, Chang C-J, et al (2017) Antibacterial cellulose paper made with silver-coated gold nanoparticles. *Sci Rep* 7:3155
66. Bouarab-Chibane L, Forquet V, Lantéri P, et al (2019) Antibacterial properties of polyphenols: Characterization and QSAR (Quantitative Structure-Activity Relationship) models. *Front Microbiol* 10:829
67. Rodríguez-León E, Iñiguez-Palomares R, Navarro RE, et al (2013) Synthesis of silver nanoparticles using reducing agents obtained from natural sources (*Rumex hymenosepalus* extracts). *Nanoscale Res Lett* 8:318
68. Golmohamadi M, Clark RJ, Veinot JGC, Wilkinson KJ (2013) The role of charge on the diffusion of solutes and nanoparticles (silicon nanocrystals, nTiO<sub>2</sub>, nAu) in a biofilm. *Environ Chem* 10:34
69. Choi O, Yu C-P, Esteban Fernández G, Hu Z (2010) Interactions of nanosilver with *Escherichia coli* cells in planktonic and biofilm cultures. *Water Res* 44:6095–6103

## Figures

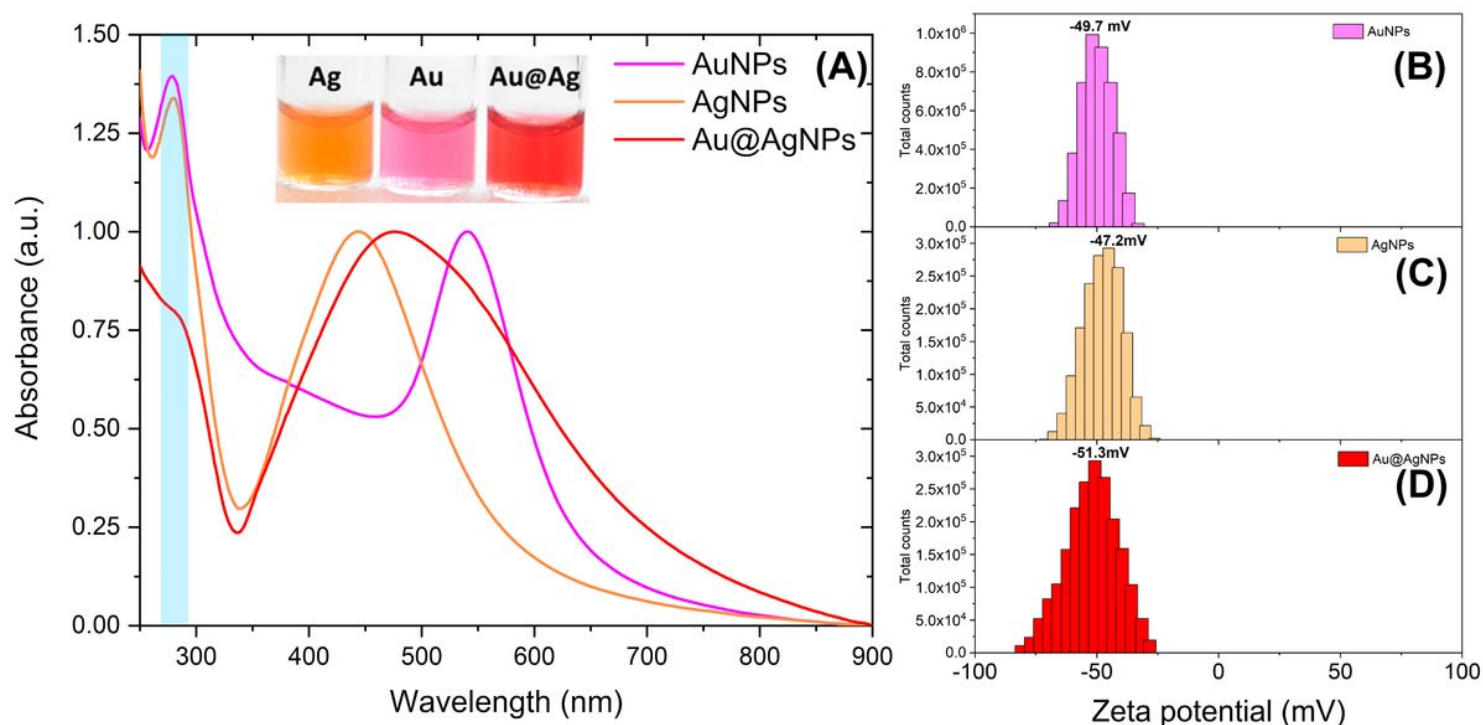


**Figure 1**

Nanoparticles UV-Vis spectra (A) and Z-Potential of Au (B), Ag (C) and Au@AgNPs (D).

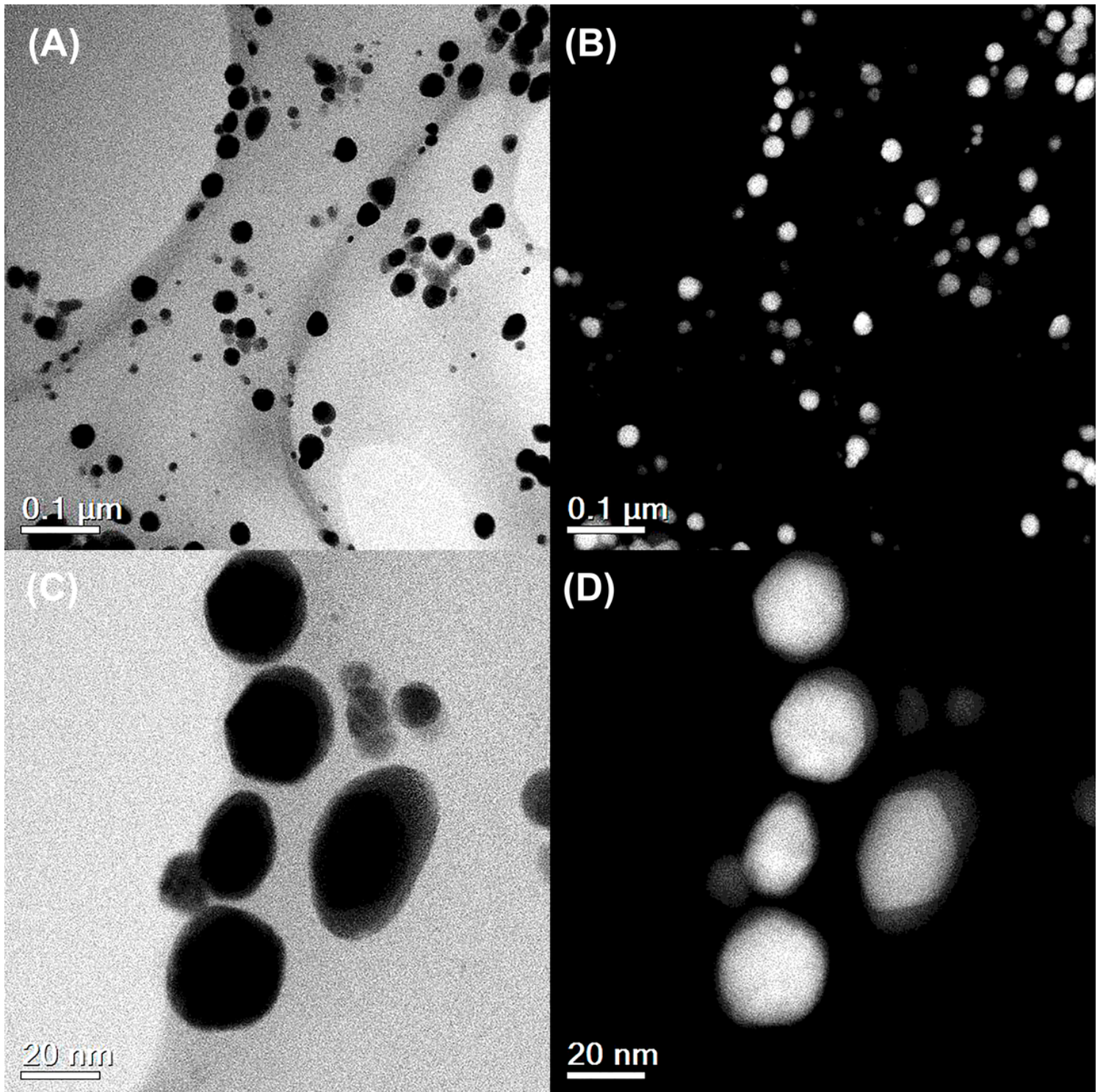


**Figure 2**

Scanning Transmission Electron Microscopy at low magnification (scale bar 100 nm) of Au@AgNPs in Bright Field (A) and HAADF (B). A Small group of Au@AgNPs at higher magnification (scale bar 20 nm) in Bright Field (C) and HAADF (D).

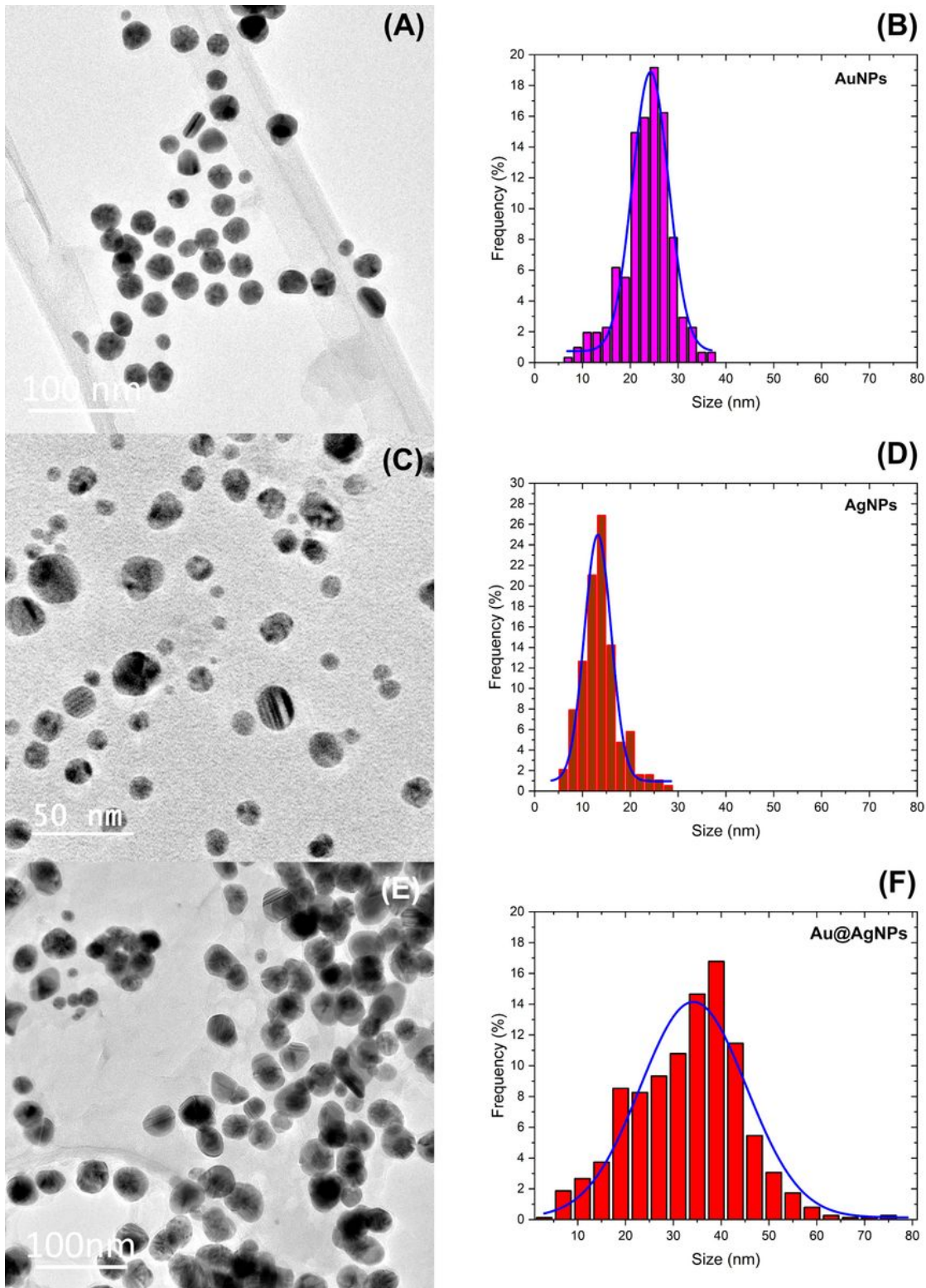


**Figure 3**

TEM and size distribution of AuNPs in (A) and (B), AgNPs in (C) and (D), and Au@AgNPs in (E) and (F).

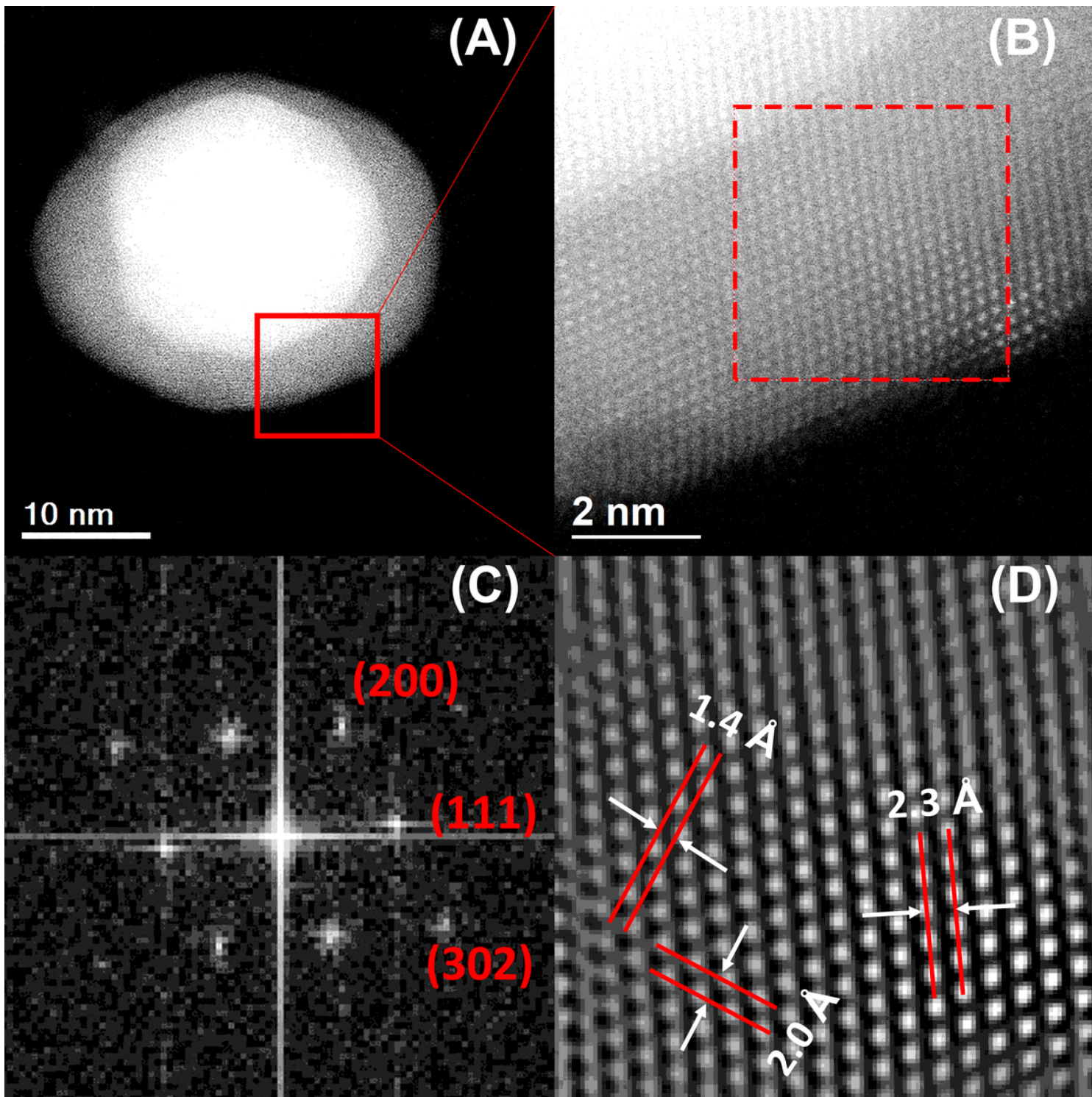
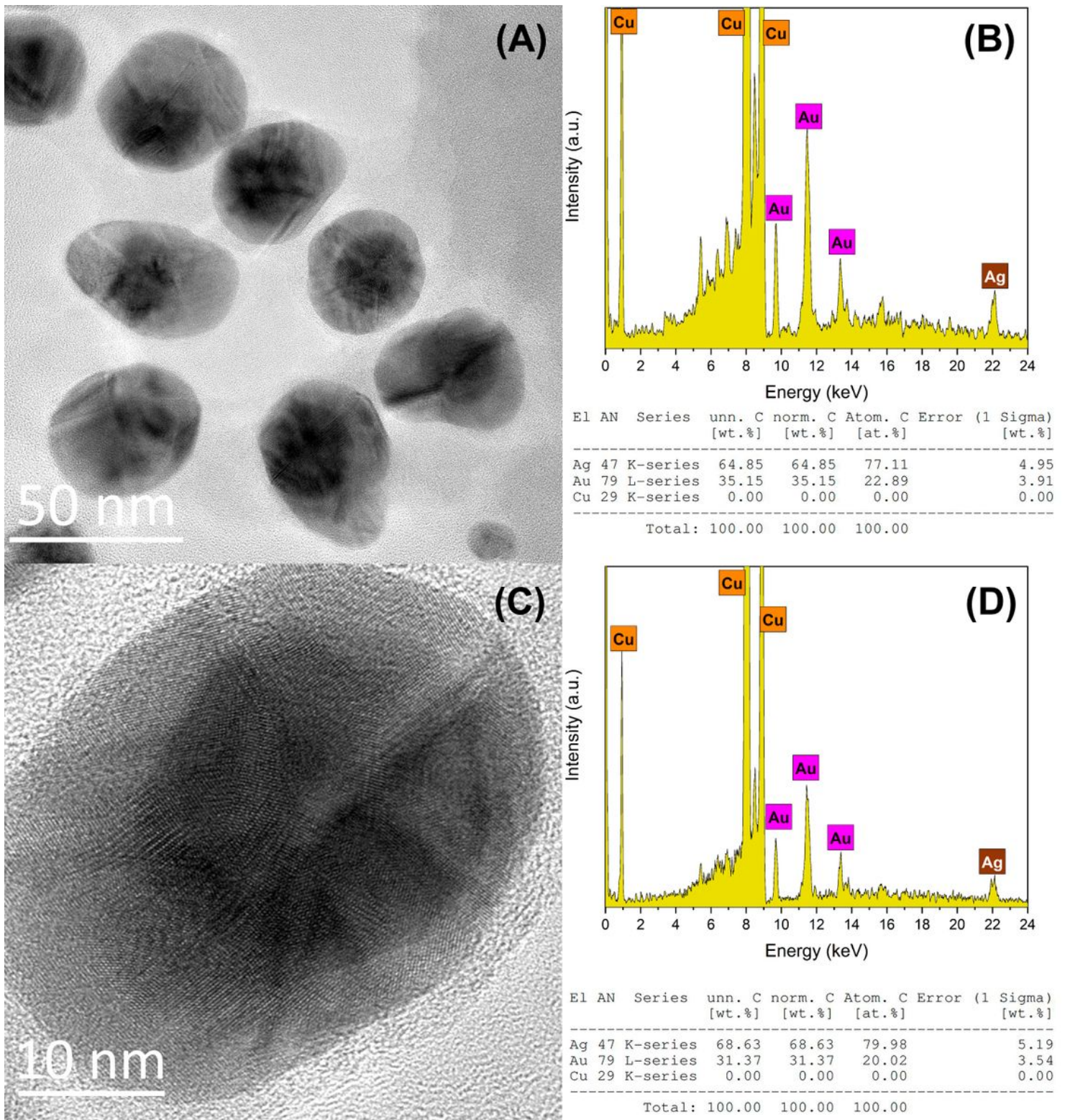


Figure 4

Au@AgNPs HRTEM (A). Magnification from (A) of interface core-shell (B). FFT plot with Miller index (C) and integrated image from FFT (Inverse) with interplanar distance (D).



**Figure 5**

TEM and EDS of an Au@AgNPs group (A-B) with Au 23 and Ag 77 % at. and single Au@AgNPs (C-D) with Au 20 and Ag 80 % at.

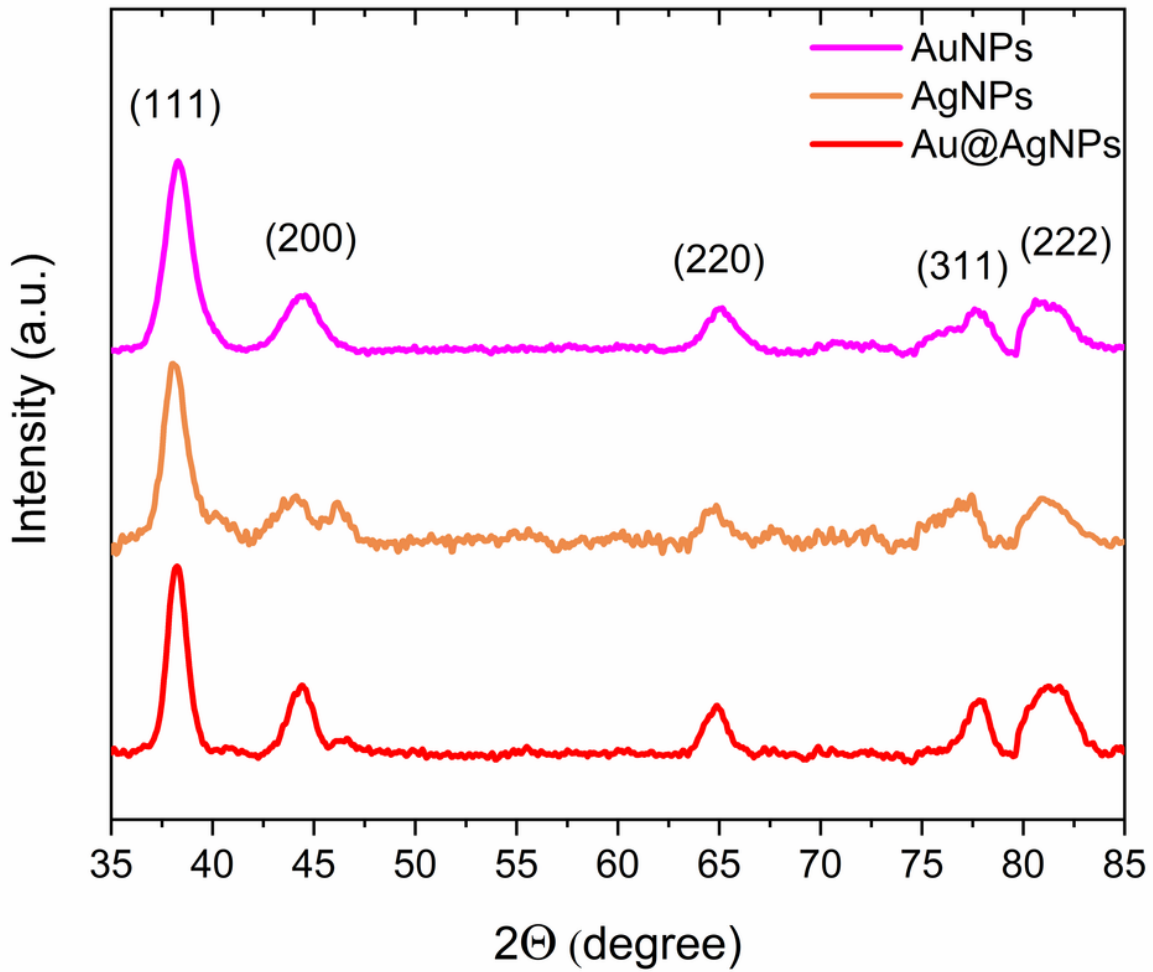


**Figure 6**

X-ray Diffraction AuNPs (pink), AgNPs (brown), and Au@AgNPs (red).



**Figure 7**

The growth curves using AuNPs, AgNPs, and Au@AgNPs like inhibitory treatments on *Candida albicans* (A-C), *Escherichia coli* (D-F), and *Staphylococcus aureus* (G-I).

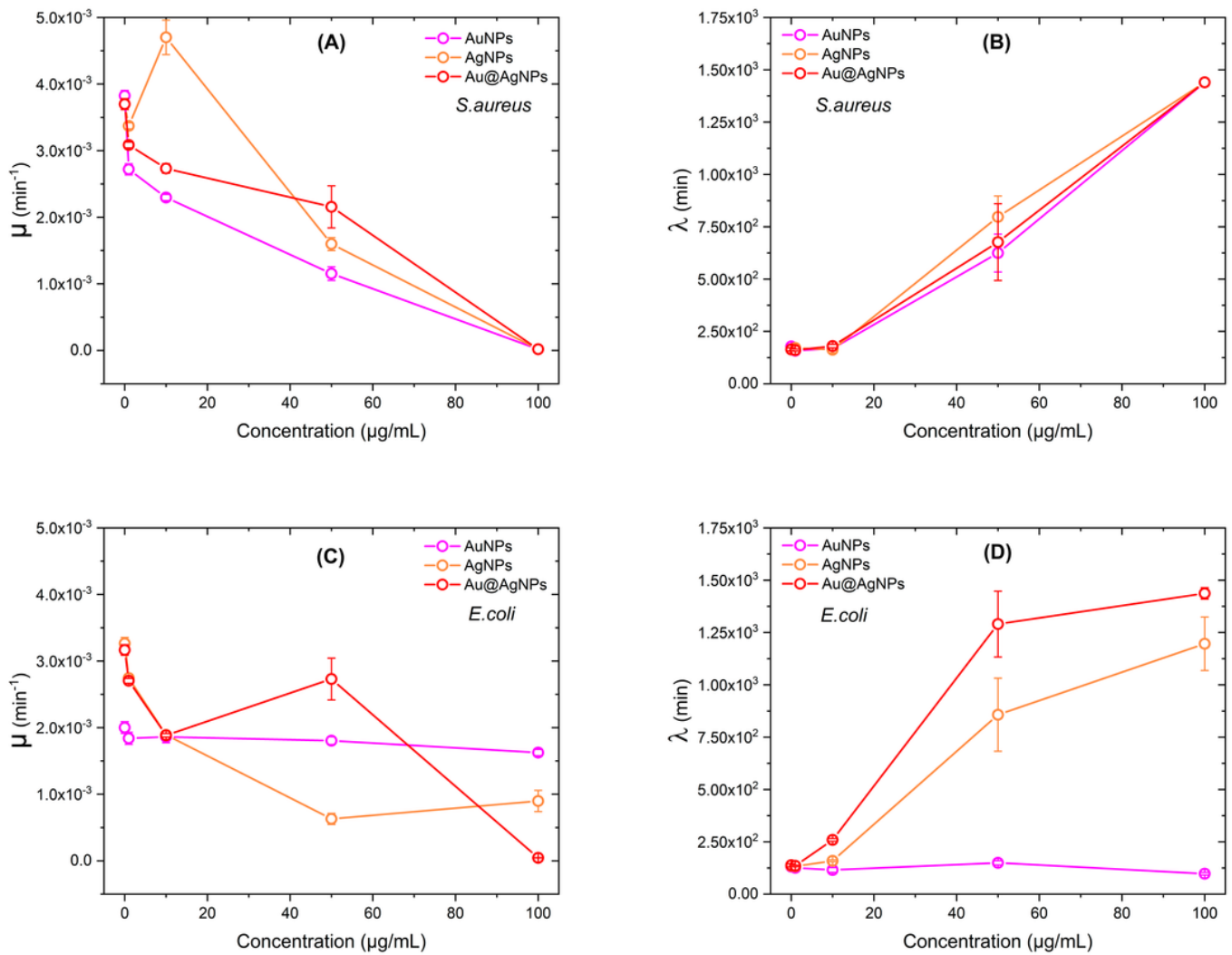


**Figure 8**

Kinetic parameters obtained by Gompertz model. Growth Rate  $\mu$  and Time Lag Phase  $\lambda$  for *S. aureus* (A and B) and for *E. coli* (C and D).

## Supplementary Files

This is a list of supplementary files associated with this preprint. Click to download.

- [SupplementarymaterialGompertzFINAL.docx](#)